Energy Materials

**Supplementary Materials**

# Boosting photoluminescence efficiency in $Yb^{3+}$-doped $CsPbCl_3$ nanocrystals via metal chloride post-treatment for high-performance luminescent solar concentrators

**Tongxin Yan[1,2], Zixuan Liu[1,2], Shuaiyao Zhang[1,2], Lei Song[1,2], Sihang Ji[1,2], Ke Xing[1,2], Jialong Zhao[3,4], Xi Yuan[1,2,*]**

[1]Jilin Provincial Key Laboratory of Wide Bandgap Semiconductor Material Growth and Device Applications, Key Laboratory of Functional Materials Physics and Chemistry of the Ministry of Education, Jilin Normal University, Changchun 130103, Jilin, China.

[2]College of Information Technology, Jilin Engineering Research Center of Optoelectronic Materials and Devices, Jilin Normal University, Siping 136000, Jilin, China.

[3]School of Physical Science and Technology, State Key Laboratory of Featured Metal Materials and Life-cycle Safety for Composite Structures, Guangxi University, Nanning 530004, Guangxi, China.

[4]Hebei Ledphor Optoelectronics Technology Co., Ltd., Baoding 071000, Hebei, China.

[*]**Correspondence to:** Prof. Xi Yuan, Jilin Provincial Key Laboratory of Wide Bandgap Semiconductor Material Growth and Device Applications, Key Laboratory of Functional Materials Physics and Chemistry of the Ministry of Education, Jilin Normal University, Changchun 130103, Jilin, China. E-mail: yuanx@jlnu.edu.cn

**ORCID:** Xi Yuan (0000-0001-8731-216X)

## EXPERIMENTAL

### Materials

Ytterbium(III) acetate tetrahydrate ($Yb(OAc)_3 \cdot 4H_2O$, 99.9%), cesium acetate (CsOAc, 99.9%), lead(II) acetate trihydrate ($Pb(OAc)_2 \cdot 3H_2O$, 99.9%), oleic acid (OA, 85% ), oleylamine (OAm, 80%-90%), chlorotrimethylsilane (TMS-Cl, ≥99.0%), and anhydrous copper(II) chloride ($CuCl_2$, 98% ) were purchased from Sigma-Aldrich. 1-Octadecene (ODE, 90%), anhydrous cadmium chloride ($CdCl_2$, 99.99%), and anhydrous nickel(II) chloride ($NiCl_2$, 99%) were obtained from Alfa Aesar. Anhydrous ethanol (99.7%) and n-hexane (99.7%) were supplied by Beijing Chemical Works. Zinc chloride ($ZnCl_2$, ≥98%) was purchased from Sinopharm Chemical Reagent Co., Ltd. Polydimethylsiloxane (Sylgard 184, PDMS) was purchased from Dow Chemical. All reagents were used as received without further purification.

### Characterization and Measurement

The crystal structure of the nanocrystals (NCs) was characterized by X-ray diffraction (XRD) on a D/max-2500 diffractometer (Rigaku, Japan) with Cu Kα radiation (λ = 0.154 nm). The XRD patterns presented in the main text were collected from NC films prepared by drop-casting a hexane dispersion of the purified NCs onto a flat sample holder, followed by drying under ambient conditions. For Rietveld refinement, XRD data were collected from dried powders of the purified NCs to minimize the influence of preferred orientation. The morphology and size of untreated and $CdCl_2$-treated Yb:$CsPbCl_3$ NCs were characterized by transmission electron microscopy (TEM) using a JEM-2100 instrument (JEOL, Japan). X-ray photoelectron spectroscopy (XPS) was performed on a Thermo Scientific Escalab 250xi (Thermo Fisher Scientific, USA) to analyze the surface elemental composition of the as-prepared perovskite NCs.

The absorption spectra were recorded using a UV-3600 spectrophotometer (Shimadzu, Japan). Steady-state photoluminescence (PL), photoluminescence

quantum yield (PLQY), PL decay curves, and temperature-dependent PL measurements were carried out on a Fluorolog-3 fluorescence spectrometer (Horiba Jobin Yvon, France) equipped with an integrating sphere, a time-correlated single-photon counting (TCSPC) module, and a vacuum cryostat (Janis VPF-500, Janis Research, USA). The UV light source used for illumination was a ZF-7 UV lamp (Anhui Ninghuai Instrument Co., Ltd., China) with a power of 6 mW and a wavelength of 365 nm. Femtosecond transient absorption (fs-TAS) measurements were performed using a Ti:sapphire laser (Astrella, Coherent, USA; 1 kHz, 800 nm) paired with a TA-100 spectrometer (Time-Tech Spectra Co., Ltd., China). A 365 nm tunable pump and sapphire-generated white-light probe were used. Pump-probe delays were tuned via an optical delay line, and ΔA signals were extracted by comparing probe spectra with and without pump light. Samples moved at 10 cm/min during measurement to prevent photodamage, and their absorption spectra remained unchanged pre- and post-test.

The photovoltaic cell was attached to one side of the luminescent solar concentrator (LSC), while the rest of the solar cell and the other three sides of the LSC were covered with black tape. The J-V curves of the LSC-PV system and the bare PV cell were measured using a source meter (Model 2400, Keithley, USA) under 100 mW/cm$^2$ AM 1.5G illumination from a solar simulator (7IS0503A, Beijing Saifan Optoelectronic Instrument Co., Ltd., China).

**Calculation of the Average Exciton Number**

Under pulsed excitation, the number of excitons initially generated in an individual NC is assumed to follow a Poisson distribution. The probability $P_i$ that an NC contains i excitons is given by[1,2]

$$P_i = \frac{\langle N \rangle^i}{i!} \exp(-\langle N \rangle) \qquad (1)$$

where i is the number of excitons generated in an individual NC and <N> is the average number of excitons generated per NC per pulse. Accordingly, the probability

that an NC contains at least one exciton is

$$1-P_0=1-\exp(-\langle N\rangle) \quad (2)$$

Assuming that the ground-state bleach (GSB) amplitude is proportional to the fraction of photoexcited NCs, its dependence on the pump photon fluence can be described as follows[1,2]:

$$-\Delta A \propto 1-\exp(-\langle N\rangle) \quad (3)$$

where $-\Delta A$ is the measured GSB amplitude. The average exciton number is related to the pump photon fluence by

$$\langle N\rangle=\sigma j_p \quad (4)$$

where σ is the absorption cross section of a single NC at the pump wavelength and $j_p$ is the incident pump photon fluence, expressed in photons $cm^{-2}$ $pulse^{-1}$. When the pump fluence F is expressed in J $cm^{-2}$ $pulse^{-1}$, $j_p$ can be calculated using

$$j_p=\frac{F}{E_{photon}}=\frac{F\lambda_{photon}}{hc} \quad (5)$$

where $\lambda_{pump}$ is the pump wavelength, h is Planck's constant, and c is the speed of light. By fitting the pump-fluence-dependent GSB amplitudes using Equation S3, the absorption cross sections were determined, from which the average exciton numbers under the TA measurement conditions were calculated.

**LSC efficiency calculation**

The calculation and extrapolation of internal optical efficiency ($\eta_{int}$) and external optical efficiency ($\eta_{ext}$) followed the protocols reported in previous literature[3-6]. Internal optical efficiency refers to the proportion of photons collected from the LSC edges relative to the total number of photons absorbed by the LSC from incident light is calculated from PLQY of the LSC ($\eta_{PL,LSC}$) and edge-emission efficiency ($\eta_{edge}$) by the following equation[3,4,6]:

$$\eta_{int}=\eta_{PL,LSC}\times\eta_{edge} \quad (6)$$

The PLQY of the LSC were measured using an integrating sphere system. The LSC edges were covered with black tape to measure the surface emission signal, while the

edge emission signal was calculated by subtracting the surface emission from the total emission. The edge-emission efficiency is determined as the proportion of edge emission relative to the total emission.

External optical efficiency corresponds to the proportion of photons emitted from the LSC edges relative to all incident photons, and can be obtained using the formula below[3-6]:

$$\eta_{ext}=\eta_{int}\times\eta_{abs} \quad (7)$$

Where $\eta_{abs}$ is the absorption ratio of the LSC device, calculated from the absorption spectrum of LSC and the photon flux spectrum of AM 1.5G.

**LSC efficiency extrapolation**

The internal optical efficiency ($\eta_{int}$) of the LSC can be expressed as follows[3]:

$$\eta_{int}=\frac{\eta_{PL}\times\eta_{trap}}{1+\beta S_2 L\left(1-\eta_{trap}\right)} \quad (8)$$

Where, $\eta_{PL}$ is the PLQY of the NCs. $\eta_{trap}$ refers to the light trapping efficiency, as defined in the equation below:

$$\eta_{trap}=\sqrt{(1-n^{-2})} \quad (9)$$

n is the LSC's refractive index. The geometric correction factor β is calculated based on the following equation:

$$\beta=1.4+0.5\left(\frac{L}{150}\right)^{\frac{1}{2}} \quad (10)$$

$S_2$ is the scattering coefficient at the PL wavelength, and L is the edge length of LSC[3,4].

$$G=\frac{L^2}{4Ld}=\frac{L}{4d} \quad (11)$$

Where G is the geometric gain of the LSC, d is the thickness of the LSC.

**Calculation of photovoltaic performance parameters**

The photovoltaic performance parameters were calculated according to the following equations[3-6]:

$$FF=\frac{P_{max}}{V_{OC}\times I_{SC}} \quad (12)$$

$$PCE=\frac{V_{OC}\times J_{SC}\times FF}{P_{in}} \quad (13)$$

FF stands for Fill Factor, and PCE stands for Power Conversion Efficiency. Where $V_{oc}$ stands for the open-circuit voltage, $I_{sc}$ denotes the short-circuit current, $J_{sc}$ represents the short-circuit current density, $P_{max}$ refers to the maximum output power, and $P_{in}$ is the incident power density of the solar simulator fixed at 100 mW/cm$^2$.

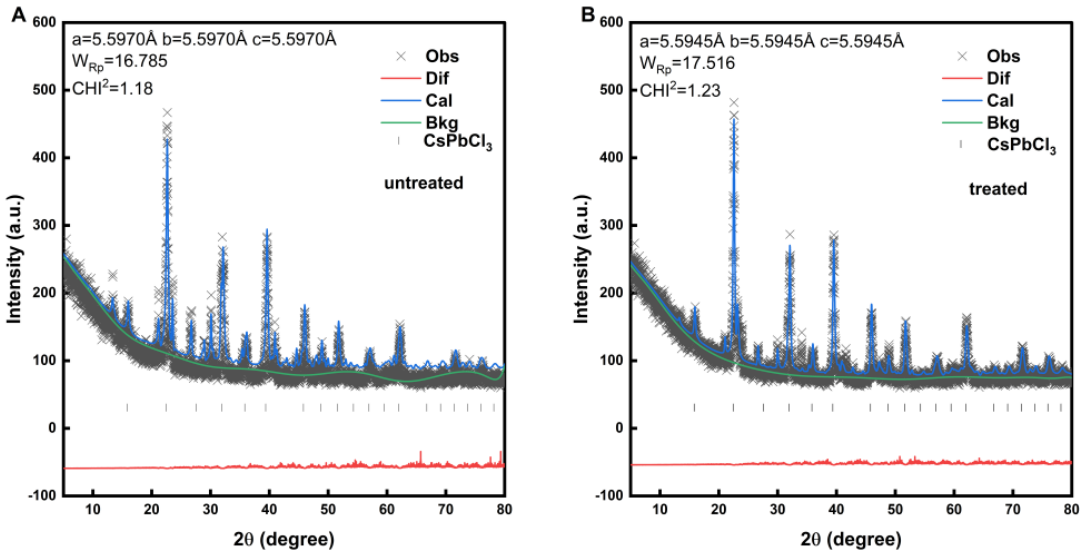


**Supplementary Figure 1.** Rietveld refinement profiles of the XRD patterns of $Yb^{3+}$-doped $CsPbCl_3$ NC powder before and after $CdCl_2$ post-treatment.

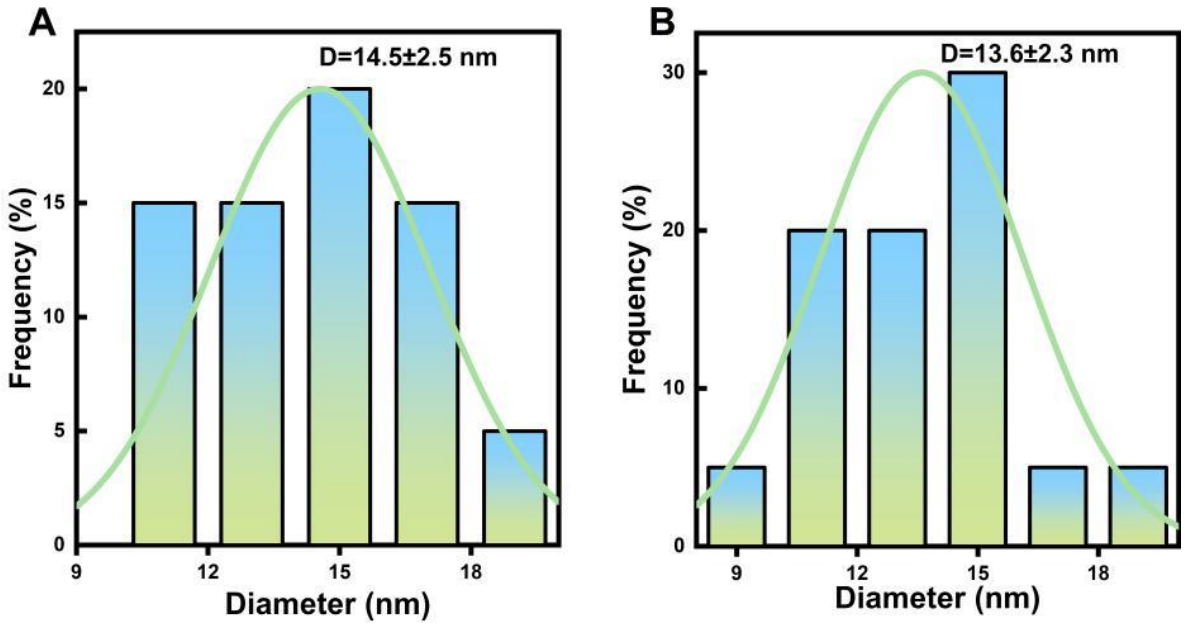


**Supplementary Figure 2.** The particle-size distribution diagrams of $Yb^{3+}$-doped $CsPbCl_3$ NCs before (A) and after (B) $CdCl_2$ post-treatment.

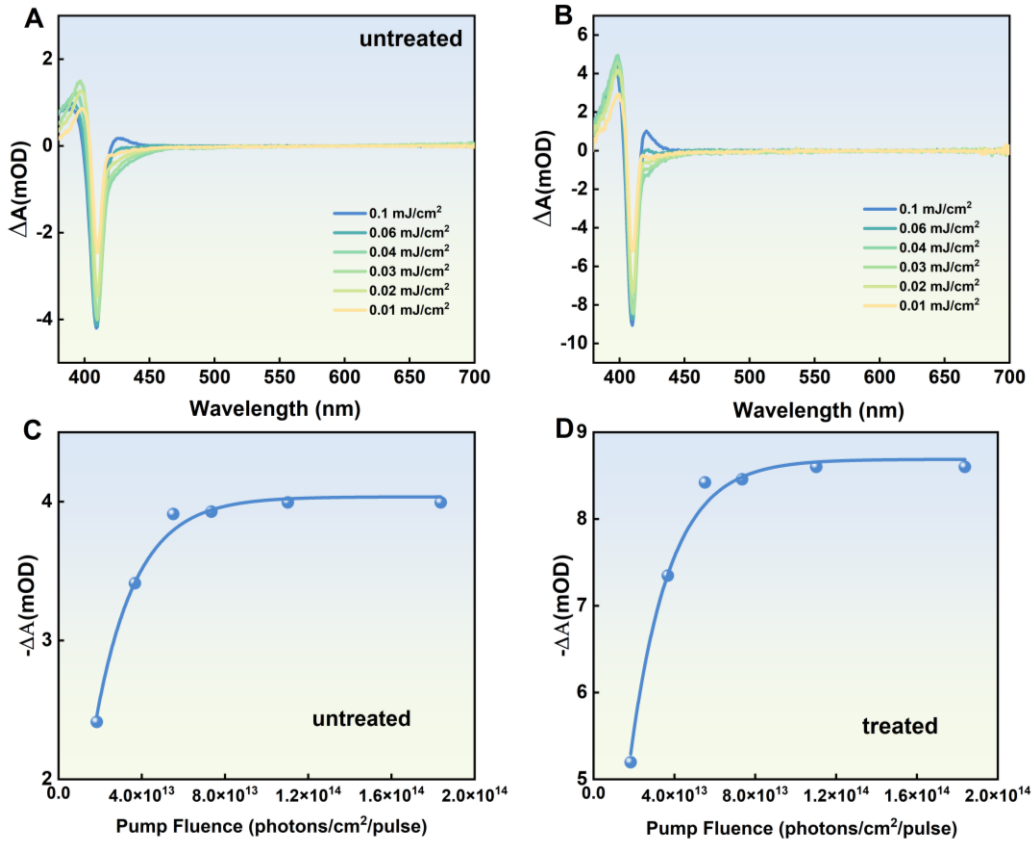


**Supplementary Figure 3.** TA of the untreated (A) and $CdCl_2$-treated (B) NCs recorded at varied pump fluences. Variations in transient absorption amplitudes of the untreated (C) and $CdCl_2$-treated (D) NCs as a function of pump photon fluence.

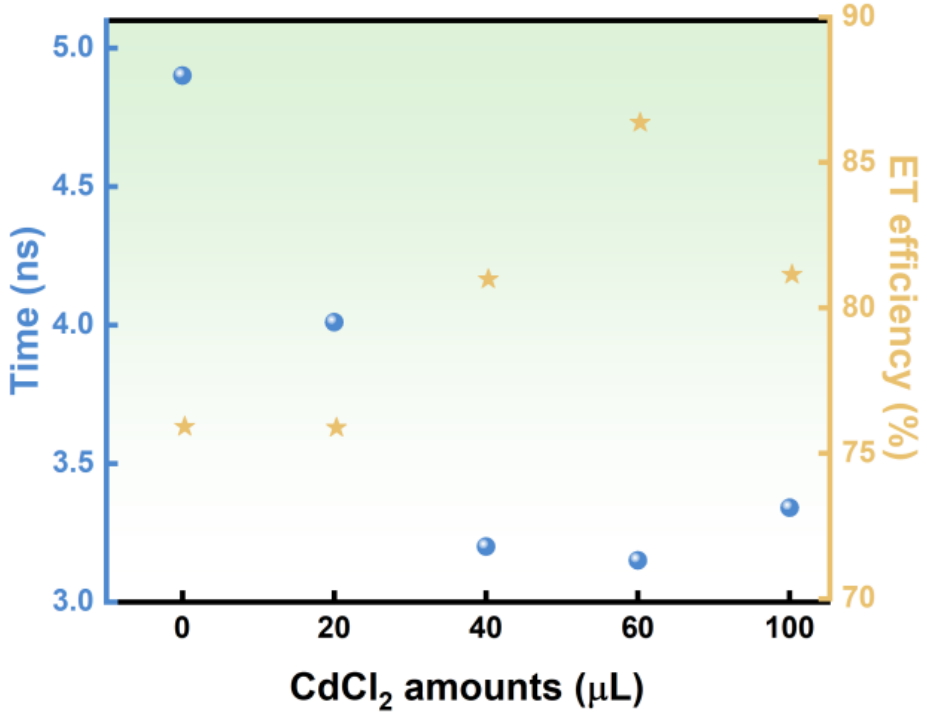


**Supplementary Figure 4.** Dependence of the host exciton lifetime and energy-transfer efficiency of $Yb^{3+}$-doped $CsPbCl_3$ NCs on the amount of $CdCl_2$.

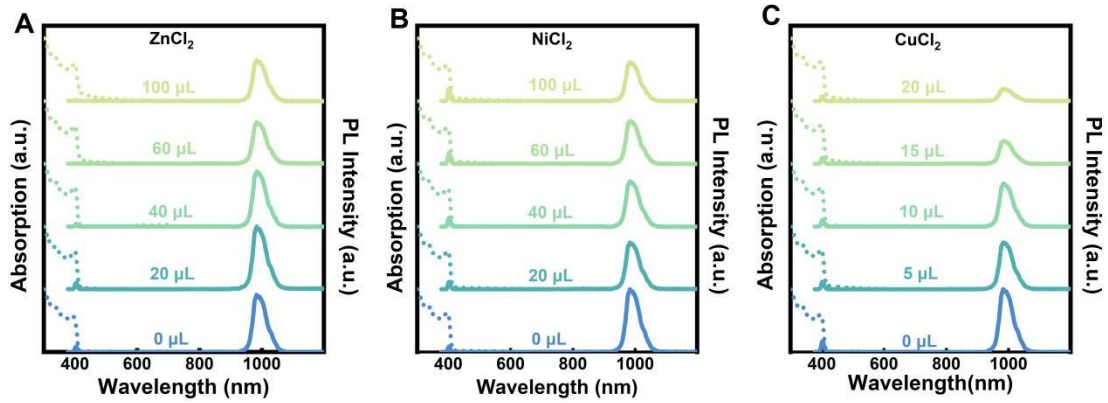


**Supplementary Figure 5.** Absorption and PL Spectra of Yb:$CsPbCl_3$ NCs treated with different amounts of $ZnCl_2$ (A), $NiCl_2$ (B), and $CuCl_2$ (C) ethanol solutions.

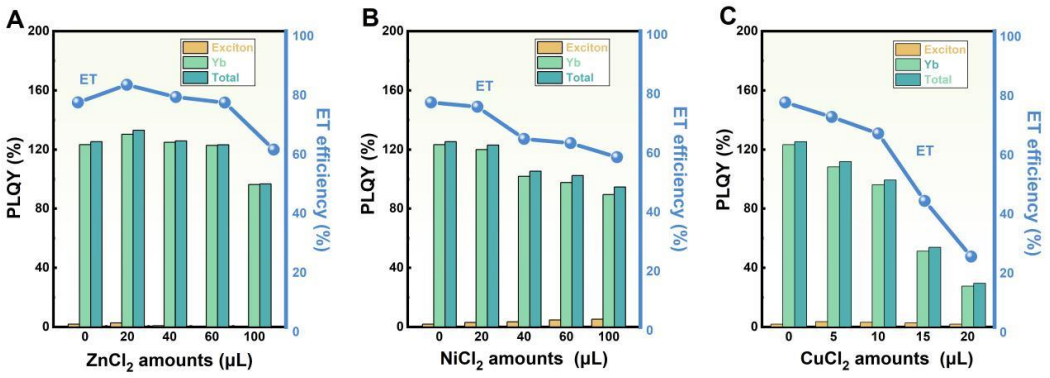


**Supplementary Figure 6.** PLQYs of the host excitonic emission, $Yb^{3+}$ near-infrared emission, and total emission, together with the exciton-to-$Yb^{3+}$ energy transfer efficiencies ($\eta_{ET}$), for Yb:$CsPbCl_3$ NCs treated with different amounts of $ZnCl_2$ (A), $NiCl_2$ (B), and $CuCl_2$ (C) ethanol solutions

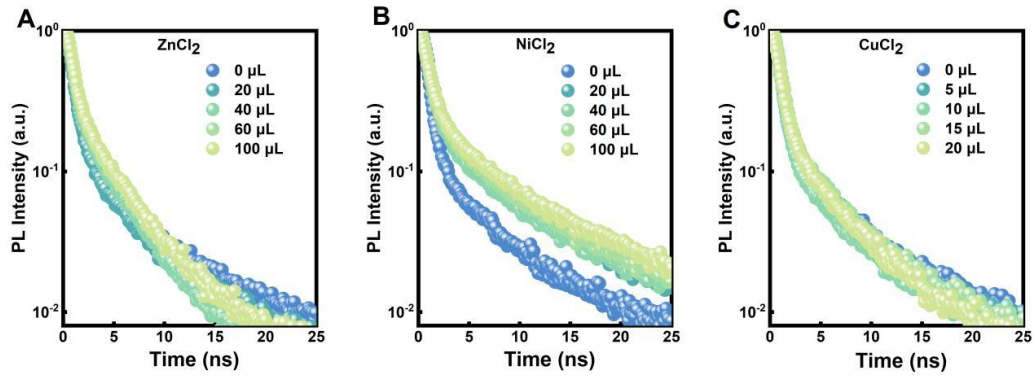


**Supplementary Figure 7.** Time-resolved PL decay curves of the host exciton emission for NCs treated with different amounts of $ZnCl_2$ (A), $NiCl_2$ (B), and $CuCl_2$ (C) ethanol solutions.

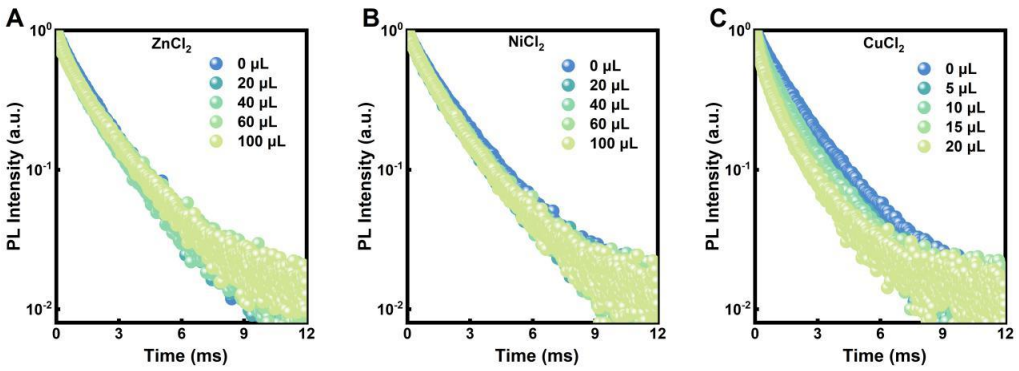


**Supplementary Figure 8.** Time-resolved PL decay curves of $Yb^{3+}$ emission for NCs treated with different amounts of $ZnCl_2$ (A), $NiCl_2$ (B), and $CuCl_2$ (C) ethanol solutions.

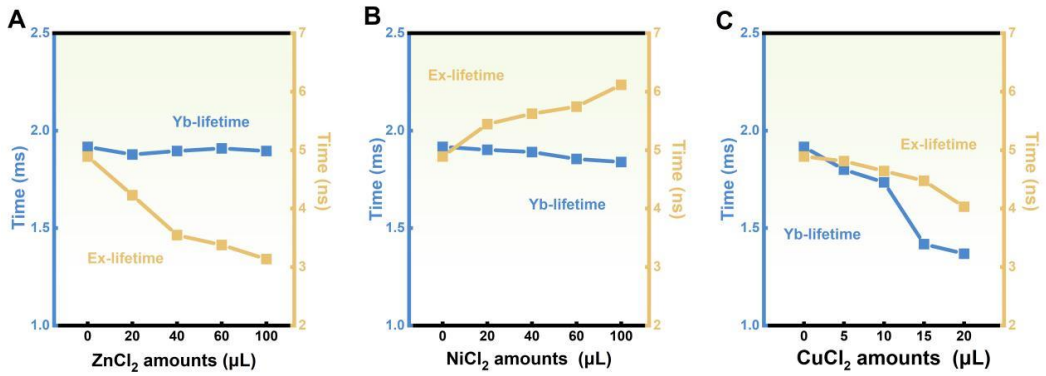


**Supplementary Figure 9.** Fitted average lifetimes of $Yb^{3+}$ and excitonic emissions for $Yb^{3+}$:$CsPbCl_3$ NCs treated with different amounts of $ZnCl_2$ (A), $NiCl_2$ (B), and $CuCl_2$ (C) ethanol solutions.

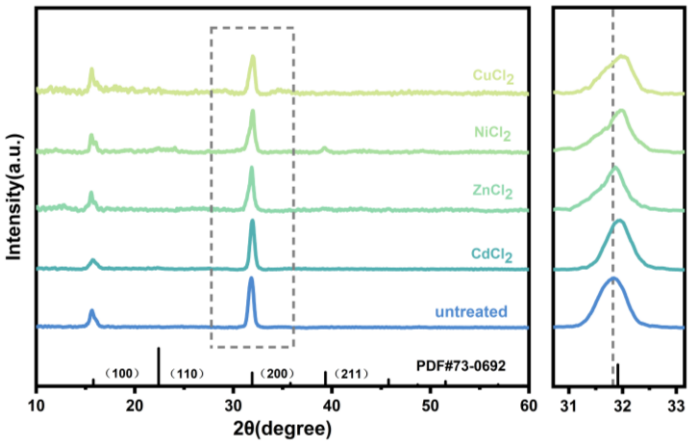


**Supplementary Figure 10.** XRD patterns of untreated and of $CdCl_2$-, $ZnCl_2$-, $NiCl_2$-, and $CuCl_2$-treated $Yb^{3+}$:$CsPbCl_3$ NCs. The inset shows the enlarged view of the (200) diffraction peak region.

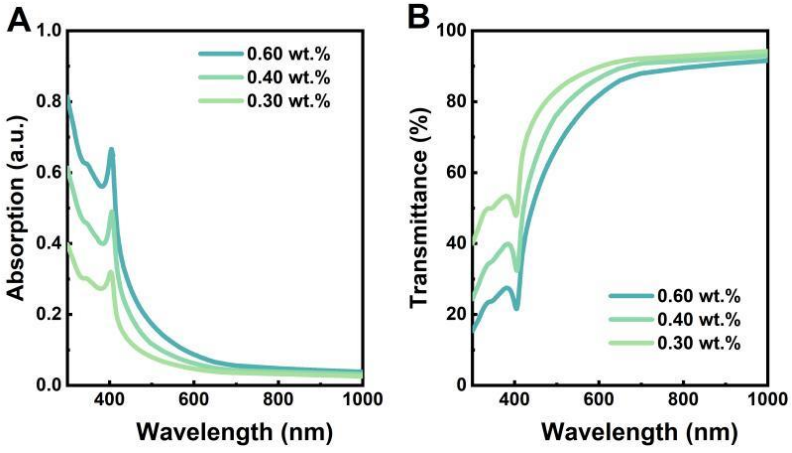


**Supplementary Figure 11.** Absorbance (A) and transmittance (B) spectra of $CdCl_2$-treated NC-LSCs with different NC concentrations.

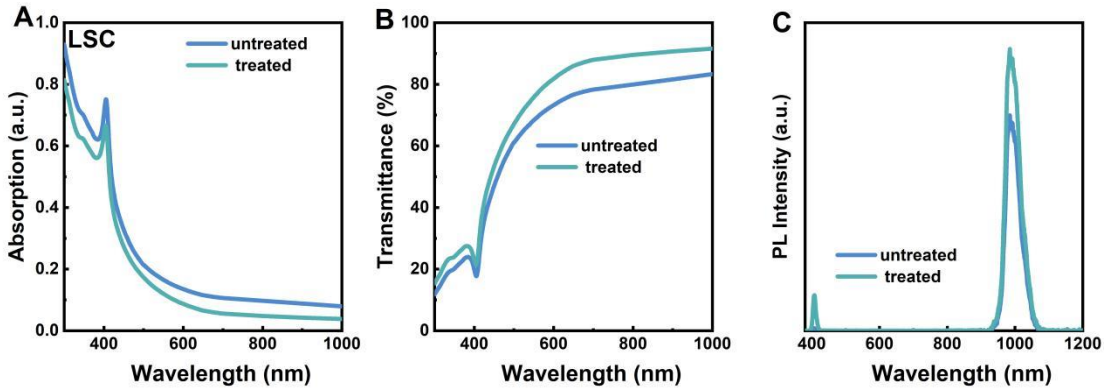


**Supplementary Figure 12.** Absorption (A), transmittance (B), and PL (C) spectra of untreated and $CdCl_2$-treated NC-LSCs.

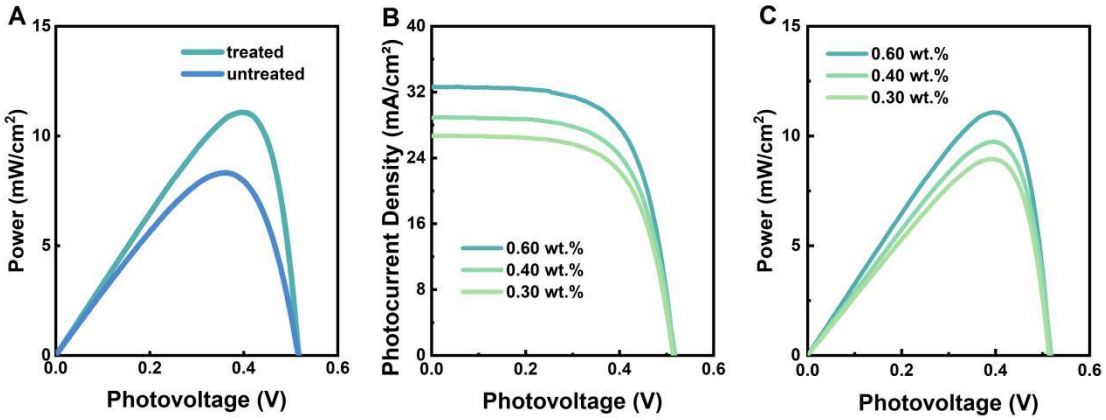


**Supplementary Figure 13.** (A) P-V curves of the silicon photovoltaic cells integrated with untreated and $CdCl_2$-treated NC-LSCs. J-V (B) and P-V (C) curves of integrated photovoltaic cells based on $CdCl_2$ treated NC-LSCs with different NC concentrations.

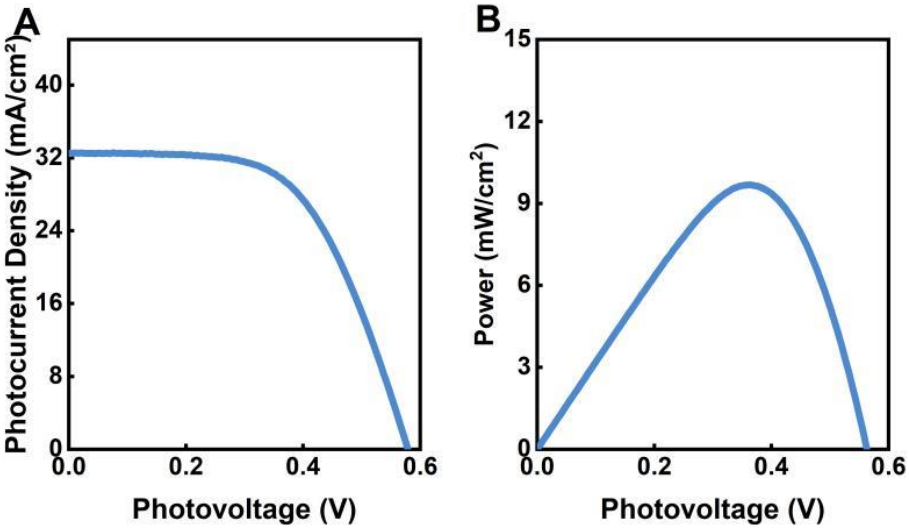


**Supplementary Figure 14.** J-V (A) and P-V (B) curves of the commercial silicon solar cell without coupling a LSC.

**Supplementary Table 1. $Yb^{3+}$ and $Cd^{2+}$ doping concentrations determined by EDS for $Yb^{3+}$:$CsPbCl_3$ NCs treated with different amounts of $CdCl_2$**

| $CdCl_2$ volumes (μL) | 0 | 20 | 40 | 60 | 100 |
|---|---|---|---|---|---|
| Yb elemental content % Yb/(Yb+Cd+Pb) | 1.72% | 1.76% | 1.75% | 1.73% | 1.75% |
| Cd element content % Cd/(Yb+Cd+Pb) | -- | 2.93% | 4.26% | 5.84% | 8.57% |

**Supplementary Table 2. Fitting results of band-gap emission decay curves for $Yb^{3+}$:$CsPbCl_3$ perovskite NCs post-treated with different amounts of $CdCl_2$**

| $CdCl_2$ (μL) | $\tau_1$ (ns) | $A_1$ | $\tau_2$ (ns) | $A_2$ | $\tau_{ave}$ (ns) |
|---|---|---|---|---|---|
| 0 | 0.98 | 0.94 | 10.45 | 0.06 | 4.90 |
| 20 | 1.17 | 0.94 | 9.65 | 0.06 | 4.01 |
| 40 | 1.61 | 0.93 | 7.47 | 0.07 | 3.20 |
| 60 | 1.96 | 0.78 | 4.86 | 0.22 | 3.15 |
| 100 | 2.03 | 0.82 | 5.50 | 0.18 | 3.34 |

**Supplementary Table 3. Fitting results of $Yb^{3+}$ emission decay curves for $Yb^{3+}$:$CsPbCl_3$ perovskite NCs post-treated with different amounts of $CdCl_2$**

| $CdCl_2$ (μL) | $\tau_1$ (ms) | $A_1$ | $\tau_2$ (ms) | $A_2$ | $\tau_{ave}$ (ms) |
|---|---|---|---|---|---|
| 0 | 0.51 | 0.20 | 2.00 | 0.80 | 1.92 |
| 20 | 0.58 | 0.22 | 2.20 | 0.78 | 2.09 |
| 40 | 0.49 | 0.18 | 2.34 | 0.82 | 2.26 |
| 60 | 0.56 | 0.18 | 2.36 | 0.82 | 2.27 |
| 100 | 0.56 | 0.08 | 2.33 | 0.92 | 2.27 |

**Supplementary Table 4. Summary of performance parameters for previously reported perovskite-based LSCs and the as-fabricated LSCs in this work**

| LSC materials | $\eta_{int}$ (%) | $\eta_{ext}$ (%) | PCE (%) | Area ($cm^2$) | Reference |
|---|---|---|---|---|---|
| $Mn^{2+}/Yb^{3+}$:$CsPbCl_3$ NCs | 76.2% | 9.6% | -- | G=3 | [3] |
| $Cs_4PbBr_6$@PMMA particles | 25.96% | 17.90% | 0.30% | 2.5 × 2.5 | [4] |
| $CsPbBr_3$ NCs | -- | 6.17% | -- | 2×2 | [5] |
| $CsPbBr_3$@$SiO_2$ particles | 44.07% | 13.68% | -- | -- | [7] |
| $Cs_2Ag_{0.4}Na_{0.6}InCl_6$ NCs | 21.2% | -- | -- | 10×10 | [8] |
| $Mn^{2+}$:$MAPbCl_3$ Pe NCs | -- | ≥8% | -- | -- | [9] |
| $Y^{3+}/Mn^{2+}$:$FAPbI_3$ NCs | -- | 17.8% | -- | 10×10 | [10] |
| $Mn^{2+}$:$FAPbI_3$ NCs | -- | 3.7% | -- | G=12.5 | [11] |
| $CsPb(Br_xI_{1-x})_3$ NCs | -- | 2% | -- | G=45 | [12] |
| Mn:$CsPbBr_3$ nanoplatelets | -- | -- | 5.28% | -- | [13] |
| $Cs_4PbBr_6$ NCs | -- | 2.4% | 1.8% | 10×10 | [14] |
| $MAPbBr_3$ NCs | 21.24% | 3.37% | -- | -- | [15] |
| $Yb^{3+}$:$CsPbCl_3$ NCs | 118.1% | 3.7% | -- | 5×5 | [16] |
| $CdCl_2$-treated $Yb^{3+}$:$CsPbCl_3$ NCs | 121.6% | 6.4% | 11.08% | 3×3 | This work |

**Supplementary Table 5. Photovoltaic parameters of the silicon photovoltaic cells integrated with untreated and $CdCl_2$-treated NC-LSCs with different NC concentrations**

| Devices | $V_{oc}$ (V) | $J_{sc}$ (mA/cm$^2$) | FF (%) | G | PCE (%) |
|---|---|---|---|---|---|
| silicon solar cell | 0.58 | 32.5 | 51.26 | -- | 9.70 |
| untreated 0.60 wt. % | 0.52 | 30.0 | 53.51 | 8.3 | 8.33 |
| treated 0.30 wt. % | 0.514 | 26.7 | 64.02 | 8.3 | 8.78 |
| treated 0.40 wt. % | 0.52 | 28.9 | 64.90 | 8.3 | 9.74 |
| treated 0.60 wt. % | 0.52 | 32.7 | 65.23 | 8.3 | 11.08 |

## REFERENCES


1. Milstein T.; Kroupa D.; Gamelin D. Picosecond quantum cutting generates photoluminescence quantum yields over 100% in ytterbium-doped $CsPbCl_3$ nanocrystals. *Nano Lett.* **2018**, *18*, 3792–3799. DOI: 10.1021/acs.nanolett.8b01066

2. Gao T.; Wei Z.; Gao S.; et al. Defect-assisted Auger recombination in graphitic carbon nitride revealed by excitation-density-dependent transient absorption spectroscopy. *Opt. Lett.* **2025,** *50,* 3792–3795. DOI: 10.1364/OL.561764

3. Cai T.; Wang J.; Li W.; et al. $Mn^{2+}/Yb^{3+}$ codoped $CsPbCl_3$ perovskite nanocrystals with triple-wavelength emission for luminescent solar concentrators. *Adv. Sci.* **2020**, *7*, 2001317. DOI: 10.1002/advs.202001317

4. Ren Z.; Deng X.; Li C.; et al. High loading $Cs_4PbBr_6$@PMMA perovskite particles for high-transmittance, ultra-stable and efficient luminescent solar concentrators. *J. Alloy. Compd.* **2025**, *1017*, 179033. DOI: 10.1016/j.jallcom.2025.179033

5. Zhang Y.; Zhang W.; Ye Y.; et al. $CsPbBr_3$ nanocrystal-embedded glasses for luminescent solar concentrators. *Sol. Energy Mater. Sol. Cells* **2022**, *238*, 111619. DOI: 10.1016/j.solmat.2022.111619

6. Kong M.; Osvet A.; Forberich K.; et al. Lead-Free Perovskite $Cs_2Ag_xNa_{1-x}Bi_yIn_{1-y}Cl_6$ microcrystals for scattering-fluorescent luminescent solar concentrators. *ACS Appl. Mater. Interfaces* **2024**, *17*, 1644–1653. DOI: 10.1021/acsami.4c18315

7. Wang X.; Wu J.; Huang D.; et al. Constructing highly efficient and ultra-stable (against Temperature, Humidity and Sunlight) luminescent solar concentrators by using dendritic $CsPbBr_3@SiO_2$ particles. *Chem. Eng. J.* **2024**, *480*, 148139. DOI: 10.1016/j.cej.2023.148139

8. Zdrazil L.; Kalytchuk S.; Langer M.; et al. Transparent and low-loss luminescent solar concentrators based on self-trapped exciton emission in lead-free double perovskite nanocrystals. *ACS Appl. Energy Mater.* **2021**, *4*, 6445–6453. DOI: 10.1021/acsaem.1c00360

9. Bhosale S.; Jokar E.; Chiang Y.; et al. Mn-doped organic-inorganic perovskite nanocrystals for a flexible luminescent solar concentrator. *ACS Appl. Energy Mater.* **2021**, *4*, 10565–10573. DOI: 10.1021/acsaem.1c01498

10. Sun C.; Wang Z.; Yang Z.; et al. Highly efficient luminescent solar concentrators based on artificial multiple quantum wells composed of $Y^{3+}$/$Mn^{2+}$co-doped $FAPbI_3$ perovskite nanocrystals. *Appl. Mater. Today* **2025**, *46*, 102887. DOI: 10.1016/j.apmt.2025.102887

11. Wang Z.; Li Z.; Qiu Z.; et al. Stable and efficient perovskite-based luminescent solar concentrators enabled by $Mn^{2+}$ doping and polymer modification of perovskite nanocrystals. *Adv. Opt. Mater.* **2025**, *13*, e00821. DOI: 10.1002/adom.202500821

12. Zhao H.; Zhou Y.; Benetti D.; et al. Perovskite quantum dots integrated in large-area luminescent solar concentrators. *Nano Energy* **2017**, *37*, 214–223. DOI: 10.1016/j.nanoen.2017.05.030

13. Luo R.; Lin T.; Chen M.; et al. Dodecylbenzenesulfonic acid-mediated synthesis of thickness-tunable Mn-Doped $CsPbBr_3$ nanoplatelets for high-efficiency luminescent solar concentrators. *Mater. Res. Bull.* **2026**, *196*, 113938. DOI: 10.1016/j.materresbull.2025.113938

14. Zhao H.; Sun R.; Wang Z.; et al. Zero-Dimensional perovskite nanocrystals for efficient luminescent solar concentrators. *Adv. Funct. Materia.* **2019**, *29*, 1902262. DOI: 10.1002/adfm.201902262

15. Li W.; Zhu J.; Zhang H.; et al. Optimizing $MAPbBr_3$ quantum dots based luminescent solar concentrators for enhanced photoelectric performance and aesthetic characteristics. *Opt. Mater.* **2025**, *162*, 116884. DOI: 10.1016/j.optmat.2025.116884

16. Luo X.; Ding T.; Liu X.; et al. Quantum-Cutting luminescent solar concentrators using Ytterbium-doped perovskite nanocrystals. *Nano Lett.* **2019**, *19*, 338–341. DOI: 10.1021/acs.nanolett.8b03966